

Composite Nanostructure Construction on the Grain Surface of Li-Rich Layered Oxides

Errui Wang, Yang Zhao, Dongdong Xiao, Xu Zhang, Tianhao Wu, Boya Wang, Muhammad Zubair, Yuqiang Li, Xueliang Sun,* and Haijun Yu*

Li-rich layered oxides (LLOs) are fascinating high-energy cathodes for lithium-ion batteries (LIBs), but still suffer from critical drawbacks that retard their practical applications. Although surface modification is effective to protect LLOs from structural deterioration, the delicate design of structures on a grain surface with promising scalability for industrial application is still challenging. Herein, using the atomic layer deposition (ALD) technique, a composite nanostructure comprising a uniform LiTaO_3 coating layer (≈ 3 nm) and a spinel interlayer structure (≈ 1 nm) is constructed on the grain surface of industrial LLO ($\text{Li}_{1.13}\text{Mn}_{0.517}\text{Ni}_{0.256}\text{Co}_{0.097}\text{O}_2$) agglomerated spheres. The surface composite nanostructure can not only enhance the structural/interfacial stability of the LLO, but also facilitates Li^+ diffusion, thereby significantly improving its cycle stability, rate performance, thermal stability, and voltage maintenance. Specifically, the LLO coated with 10 ALD cycles exhibits a small voltage decay rate of 0.9 mV per cycle, a reversible capacity of 272.8 mAh g^{-1} at 0.1 C, and a capacity retention of 85% after 200 cycles at 1 C, suggesting the important role of surface composite nanostructure for improving the electrochemical performance. This work provides new insights into the composite nanostructure design on the grain surface of cathode materials for high-performance LIBs.

promising battery family for these goals. However, the unsatisfying performance of LIBs, largely constrained by cathodes, still impedes their further applications. Among various cathode materials, lithium-rich layered oxide materials (LLOs), formularized as $x\text{Li}_2\text{MnO}_3 \cdot (1-x)\text{LiTMO}_2$ ($0 < x < 1$, TM = transitional metals, such as Ni, Co, and Mn), have attracted wide attentions owing to their superior reversible capacity, high operating voltage and low cost.^[1–5] However, LLOs, particularly the industrial applicable agglomerated micrometer-scale spheres, still suffer from key obstructions, such as the fast voltage decay, poor capacity retention, low rate capacity and unsatisfying safety,^[6–8] which are partially originated from the cathode structural deterioration and interfacial side reactions. In particular, side reactions result in many drawbacks such as the growth of non-conductive cathode electrolyte interphase (CEI), the increase of electric resistance, the TM dissolution, the corrosion, and cracking of spheres,

The strong market incentives and pressing environmental preservation call for high-energy, eco-friendly, and high-safety batteries. Lithium-ion batteries (LIBs) are still the most

among others.^[9–11] Moreover, the thermal stability of LLOs is important to guarantee their safety. It is thus crucial to optimize LLOs, especially agglomerated spheres, by industrially available approaches to realize superior cycle/thermal stability, high rate performance, and minor voltage decay for practical applications.

Many strategies have been proposed to adjust the structures of LLOs to overcome the above drawbacks, including the local-structure control,^[8] elemental doping,^[12,13] crystal domain design,^[7] surface modification,^[14,15] and their combinations.^[16] Among them, the construction of protective surface structures is effective to suppress side reactions, improve the structural stability, and promote the Li^+ diffusions across interface. From a structure perspective, LLOs have been identified to comprise of “twin-domain” structures, including LiTMO_2 and Li_2MnO_3 crystal domains with different functions.^[17,18] A further integration of compatible spinel structures at the LLO’s grain surface, either by post introduction or in situ growth, may provide new functional units to improve the rate performance of LLOs.^[19,20] The effects of spinel structure are highly dependent on their intrinsic properties and integrated configurations with LLOs. However, spinel structure often appears as irregular particles or

E. Wang, Prof. X. Zhang, T. Wu, B. Wang, M. Zubair, Y. Li, Prof. H. Yu
Faculty of Materials and Manufacturing
Key Laboratory of Advanced Functional Materials
Education Ministry of China
Beijing University of Technology
Beijing 100124, P. R. China
E-mail: hj-yu@bjut.edu.cn

Dr. Y. Zhao, Prof. X. Sun
Department of Mechanical and Materials Engineering
University of Western Ontario
London, Ontario N6A 5B8, Canada
E-mail: xsun@eng.uwo.ca

Prof. D. Xiao
Beijing National Laboratory for Condensed Matter Physics
Institute of Physics
Chinese Academy of Sciences
Beijing 100190, China

 The ORCID identification number(s) for the author(s) of this article can be found under <https://doi.org/10.1002/adma.201906070>.

DOI: 10.1002/adma.201906070

relatively thick layers, which may decrease the overall capacities. The precise and facile control of spinel structures in terms of morphology, thickness, oriented growth is thus crucial, but still challenging. On the other hand, for the post construction of a shell-like coating layer, many methods such as sol-gel encapsulation,^[21] hydrothermal synthesis,^[22] and sputtering deposition^[23] have been applied, but can hardly provide well-defined, ultra-uniform, and ultrathin structures in large scale. In contrast, the gas-phase atomic layer deposition (ALD) favors high-throughput and ultra-uniform coating on not only LLO nanostructures but also industrial applicable micrometer-scale spheres at relatively low temperatures.^[24–26] Although ionic insulative metal oxides such as Al_2O_3 ^[27] and TiO_2 ^[27,28] have been commonly used in ALD process, it would be essential to explore ionic conductive coating materials in ALD process, which is more challenging but more effective to improve the Li^+ transfer as well as to suppress side reactions.

Herein, a composite nanostructure comprising of an ultra-uniform and ultrathin LiTaO_3 coating shell (≈ 3 nm) and specifically grown spinel interlayers (≈ 1 nm), has been fabricated using ALD on an industrial applicable LLO ($\text{Li}_{1.13}\text{Mn}_{0.517}\text{Ni}_{0.256}\text{Co}_{0.097}\text{O}_2$). Combining the advanced atomic-resolution high-angle annular dark-field scanning transmission electron microscopy (HAADF-STEM) and spectroscopy techniques, the composite nanostructure on grain surface of LLO has been clearly revealed. Furthermore, experimental studies on these modified LLOs have confirmed their enhanced electrochemical performance. The ALD-coated LLOs, especially the LLO treated with 10 cycles, exhibit small voltage decay, significantly enhanced cycle/thermal stability, and promising rate performance. The mechanism of the performance improvement was also disclosed experimentally and theoretically, shedding lights on the delicate control of structures on grain surface of LLOs for superior performance toward practical applications.

The pristine $\text{Li}_{1.13}\text{Mn}_{0.517}\text{Ni}_{0.256}\text{Co}_{0.097}\text{O}_2$ (P-LLO) was synthesized by a co-participation method. ALD processes were then performed on P-LLO using two LiTaO_3 precursors including $(\text{CH}_3)_3\text{COLi}$ and $\text{Ta}(\text{OC}_2\text{H}_5)_5$ to produce a series of modified LLOs- n , where n stands for the number of ALD cycles. The influence of ALD process on the structure of LLOs was first evaluated by morphologic investigation using scanning electron microscopy (SEM). As shown in Figure 1a, P-LLO appears as regular spheres with an average diameter of around 10 μm , which are tightly agglomerated by semi-cubic primary particles with sizes of 100–150 nm (Figure 1b). The tiny channels between primary nanoparticles in spheres were formed by CO_2 bubbling during the decomposition of carbonate precursors at high temperatures.^[13] The as-modified LLOs- n well maintained the spherical morphology (Figure 1d and Figure S1, Supporting Information). However, an n -dependent surface densification of LLOs- n can be clearly observed (Figure 1c and Figure S2, Supporting Information), indicating the continuous coating of LiTaO_3 onto P-LLO. The elemental distributions at LLOs- n surfaces were disclosed by energy dispersive X-ray spectroscopy (EDS) (Figure 1d–h and Figure S1, Supporting Information), showing that Ni, Co, and Mn elements were uniformly distributed in P-LLO and LiTaO_3 -coated LLOs- n . In addition, Ta was found to distribute uniformly on LLOs- n , suggesting the fine coating of LiTaO_3 onto the P-LLO. The crystal structures

of these P-LLO and LLOs- n were examined by X-ray diffraction (XRD), as shown in Figure 1i. For all the tested materials, most peaks can be well indexed to an $\alpha\text{-NaFeO}_2$ crystal domain (space group $R\bar{3}m$), while the weak ones between 20° and 23° are originated from the Li_2MnO_3 -like crystal domain (space group $C/2m$) in LLOs.^[12,13,18,29,30] The significant splitting of (006)/(102) and (018)/(110) peaks indicates the highly-ordered layered structures of these materials.^[31] Significantly, P-LLO and LLOs- n show no difference in XRD patterns, suggesting that the ALD processes did not alter the intrinsic crystal structure of P-LLO.

To clearly reveal the surface structure of LLOs- n induced by ALD process, LLO-10 was adopted as a representative and investigated by TEM. It can be seen that an ultrathin LiTaO_3 layer with a uniform thickness of ≈ 3 nm was fabricated in Figure 1j and Figure S3, Supporting Information. HAADF-STEM was further carried out to scrutinize the surface atomic structures. As shown in Figure 1k, the surface regions of LLOs contain three kind of structures: 1) layered “twin domain” structure is maintained in the bulk; 2) an ultrathin spinel interlayer structure (≈ 1 nm) was preferentially grown along the [120] direction of LLO-10 underneath the LiTaO_3 layer; 3) amorphous LiTaO_3 layer with a thickness of ≈ 3 nm is clearly seen as the outermost shell of spheres. The element distributions of Mn, Ni, Co, Ta, and O were revealed by STEM-EDS mapping (Figure S4, Supporting Information), and the observed Ta signals agree with the formation of LiTaO_3 layer.^[32–34] The mass fraction of Ta measured by ICP was estimated to be 0.45%. In order to figure out the Li^+ diffusion kinetics of the LLO-10 surface, Li^+ migration barrier energy was calculated by density functional theory (DFT) (Figure 1l), according to the possible lithium diffusion paths in spinel and Li_2MnO_3 structures (Figure S5, Supporting Information). The result shows Li^+ migration barrier energies in Li_2MnO_3 structure and spinel structure are 0.62–0.84 and 0.36 eV, respectively, demonstrating that the existence of spinel interlayer structure can promote the Li^+ diffusion kinetics. The surface structures noticeably influence the interfacial chemistry of LLOs, which can be clarified by X-ray photoelectron spectroscopy (XPS).^[15,35] To distinguish the different chemical structures of LLOs before and after ALD coating, P-LLO and LLO-10 were analyzed by XPS technique. Figure 2a shows the surveyed spectra of P-LLO and LLO-10 after calibration. It was found that the Mn 2p, Ni 2p, and Co 2p spectra have slight shifts after ALD coating (Figure 2b–d), demonstrating the TM ions were slightly reduced. Owing to the coating LiTaO_3 layer, LLO-10 exhibits noticeable Ta 4f peaks in Figure 2e. The chemical valence of Ta was determined to be +5 from the binding energies of Ta 4f at 28.1 and 25.6 eV, in line with the designated chemical states of LiTaO_3 .^[36,37] In addition, the relative intensities of Mn/Ni/Co-O peaks peak in O 1s spectra (Figure 2f) decrease from 68% to 65.1%, implying that LiTaO_3 was deposited on LLO-10.

To evaluate the ALD-adjusted surface structure on the performances, a series of electrochemical measurements were carried out. Figure 3a shows the initial charge–discharge curves of LLOs at a current density of 0.1 C (20 mA g^{-1} , 1 C = 200 mA g^{-1}) from 2.0 to 4.8 V at 25 $^\circ\text{C}$. The discharge specific capacities of P-LLO, LLO-2, LLO-5, LLO-10, and LLO-20 in the first cycle were 269.4, 271.0, 272.0, 272.8, and 253.2 mAh g^{-1} , with the corresponding Coulombic efficiencies (CEs) to be 79.39%, 82.1%,

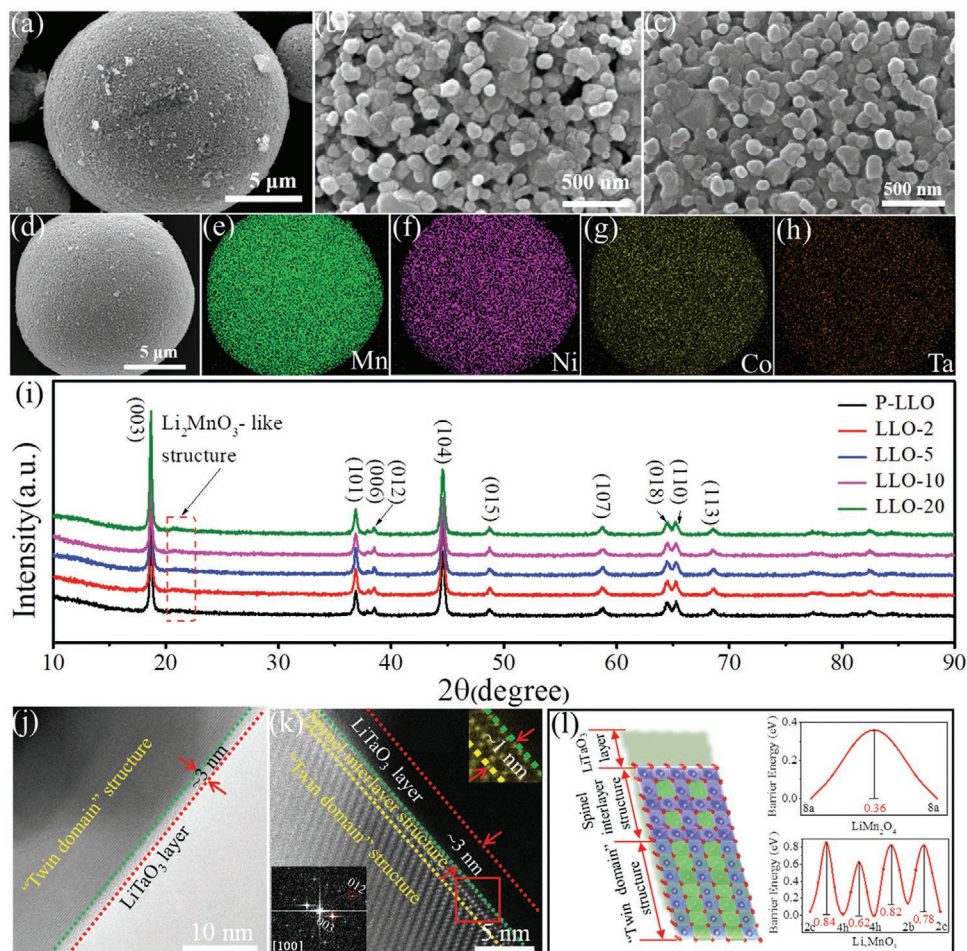


Figure 1. a) Large-scale and b) high-resolution SEM images of P-LLO. c) High-resolution SEM image of LLO-10. d) Large-scale SEM image and e–h) EDS images of LLO-10 showing the elemental distributions of Mn (e), Ni (f), Co (g), and Ta (h). i) XRD patterns of P-LLO and LLOs-*n*. j) TEM image shows the ALD-coated layer of LLO-10. The green dotted line represents the interface between the LiTaO₃ layer and spinel interlayer structure, and the red dotted line represents the surface of LiTaO₃ layer. k) HAADF-STEM image of LLO-10. FFT pattern of the interlayer structure reflection projected along [100] direction and magnified area of the red rectangle are shown as insets. The yellow dotted line represents the interface between the “twin domain” structure of LLOs and the spinel interlayer structure. l) The structure model of LLO-10 (left) and the diffusion barrier energies of Li⁺ in spinel structure and “twin domain” structure (right).

82.69%, 83.72%, and 79.49%, respectively. Figure 3b shows the long-cycle performance of all cathodes at 1 C from 2.0 to 4.6 V at 25 °C. The capacity retentions of P-LLO, LLO-2, LLO-5, LLO-10, and LLO-20 after 200 cycles were 64.2%, 75.5%, 80.4%, 85%, and 81.7%, respectively. It can be concluded that the capacity, CE and capacity retention of these materials were improved with the increase of *n* when *n* is below 10. However, the ALD coating for 20 cycles led to a reverse trend. The capacity, CE and capacity retention of LLO-20 were lower than those of LLO-10. The increase of *n* can effectively reduce side reactions at electrode/electrolyte interfaces and thus improve the reversible Li⁺ migration process, but increase the electrochemical polarization of the cathode when *n* is too large (Figure S6a, Supporting Information). The contradictory effects of ALD cycles *n* would request an elegant and balanced adjustment, as the case of the optimal LLO-10 among these materials.

A major challenge of LLOs as practical cathode materials is the fast discharge voltage decay during cycling. Figure 3c and

Figure S6, Supporting Information show that the ALD coating significantly suppresses the average voltage decay. For example, the voltage of P-LLO decreases from 3.65 to 3.26 V after 200 cycles ($\Delta V = (V_{\text{first}} - V_{200\text{th}})/200 \text{ cycle} = 1.95 \text{ mV per cycle}$), whereas that of LLO-10 only decreases to 3.47 V ($\Delta V = 0.9 \text{ mV per cycle}$, a relatively minor value for reported LLOs, Table S1, Supporting Information). The voltage decay dominantly occurs at low voltages, as also observed in Figures S7 and S8, Supporting Information. Obviously, LLO-10 show less shift of the Mn⁴⁺ reduction peak (peak *p* in Figure S8, Supporting Information) to the lower voltage, as indicated by the red dotted squares, in sharp contrast to P-LLO. LLO-10 with less voltage decay suggests that the uniform surface composite nanostructure protect the surface structure of LLO from degradation.

As the optimal cathode, LLO-10 was adopted in the following studies. By comparing with P-LLO, it can be seen that the LiTaO₃ layer and spinel interlayer structure induced by ALD process can improve the rate capability (Figure 3d). LLO-10

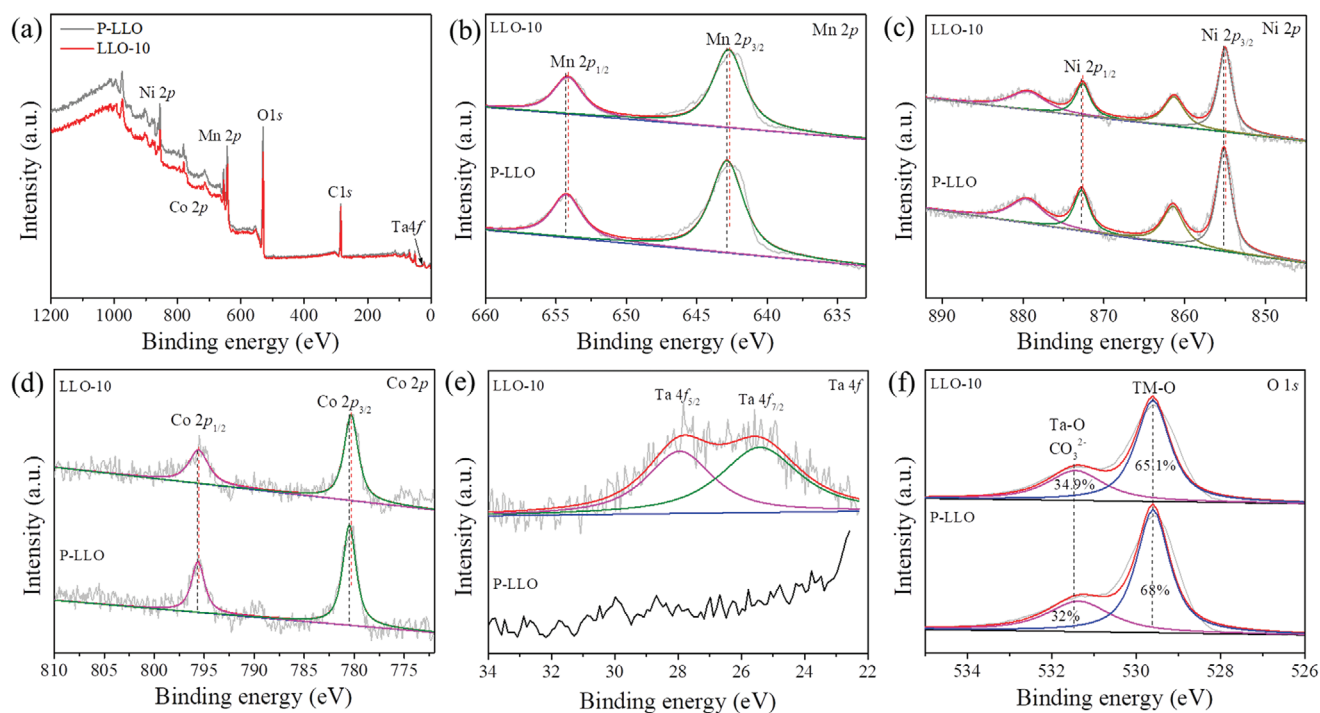


Figure 2. a) XPS survey spectra of P-LLO and LLO-10. b) Mn 2p, c) Ni 2p, d) Co 2p, e) Ta 4f, and f) O 1s spectra of P-LLO and LLO-10.

delivered higher discharge capacities of 273.2, 261.7, 235.5, 218.4, 193.5, and 153.2 mAh g⁻¹ at 0.1, 0.2, 0.5, 1, 2, and 5 C, respectively, in sharp contrast with those of P-LLO (266.7, 235.6, 209.1, 185.4, 160.8, and 130.7 mAh g⁻¹). Such a good rate performance suggests the enhancement of kinetics of LLO-10, which is likely attributed to the LiTaO₃ layer and spinel interlayer structure with 3D fast Li⁺ diffusion channels as well as the minimized parasitic reactions at interface. We thus monitored the parasitic reactions by measuring the CE of the battery. The average CEs of P-LLO and LLO-10 is <99.4% and >99.6% (Figure S9, Supporting Information), respectively, indicating significant improvement by surface modification. In addition, cycle stability measured at elevated temperatures is requested since the side reactions would speed up at elevated temperatures. The P-LLO and LLO-10 electrodes were cycled at 1 C for 60 cycles at 55 °C, both of which deliver improved discharge capacities in comparison with those at 25 °C (Figure 3e). Specifically, the LLO-10 exhibits a high capacity (245.7 mAh g⁻¹) and excellent capacity retention (90.4%). The thermal stability of LLOs in charge states is important for the safety of practical batteries. Differential scanning calorimetry (DSC) tests were conducted under Ar atmosphere to evaluate the changes of the thermal behavior before and after ALD coating. It can be seen from Figure 3f that the P-LLO has a main exothermic peak at 269.75 °C, which is increased to 290.3 °C for LLO-10. The heat generation is thus reduced from 287.66 J g⁻¹ for P-LLO to 192.5 J g⁻¹ for LLO-10, suggesting the improved thermal stability for the latter. This is likely owing to the suppression of LLO degradation by the protection of the LiTaO₃ layer and spinel interlayer structure.

Moreover, the electrochemical performance of LLOs in full cells provides more reliable information for practical batteries,

and thus the performances of P-LLO and LLO-10 were also tested in full cells using graphite as the anode (Figure 3g). It can be seen that LLO-10 exhibits a better capacity retention of 78% at 1 C after 350 cycles than P-LLO (56.7%). The corresponding discharge profiles of P-LLO show noticeable voltage decay with increased cycling (Figure S10, Supporting Information). In contrast, the voltage decay is effectively suppressed after ALD process. More importantly, the LLO-10/graphite full cell displayed a specific capacity of 151.7 mAh g⁻¹ at 5 C (Figure S11, Supporting Information). The energy densities of P-LLO and LLO-10 upon cycling in full cells are displayed in Figure S12, Supporting Information. LLO-10 can deliver a higher first-cycle energy density of 970.1 Wh kg⁻¹ at 0.1 C and an energy density retention of 71.8% after 350 cycles. In contrast, the P-LLO electrode can deliver a lower first-cycle energy density of 908 Wh kg⁻¹, and a poor energy density retention of 55.6% after 350 cycles. Furthermore, the discharge power density of the LLO can also be enhanced after ALD coating (Figure S13, Supporting Information). These results suggest that the composite nanostructure modification by ALD method can stabilize the interphase of the LLO and suppress side reactions, and thus effectively improve the cycle stability, rate performance, and safety. For comparison, some representative methods for the optimization of electrochemical performance of LLOs are listed in Table S1, Supporting Information. It can be clearly observed that our ALD coating with LiTaO₃ layer leads to a relatively good performance. Especially, the rate capacity of LLO-10 at 5 C is significantly high, and the voltage decay rate (0.9 mV per cycle) is very small.

The parasitic reactions at the electrode–electrolyte interface can lead to the accumulation of side products and the increase of impedance during cycling. To understand the interfacial

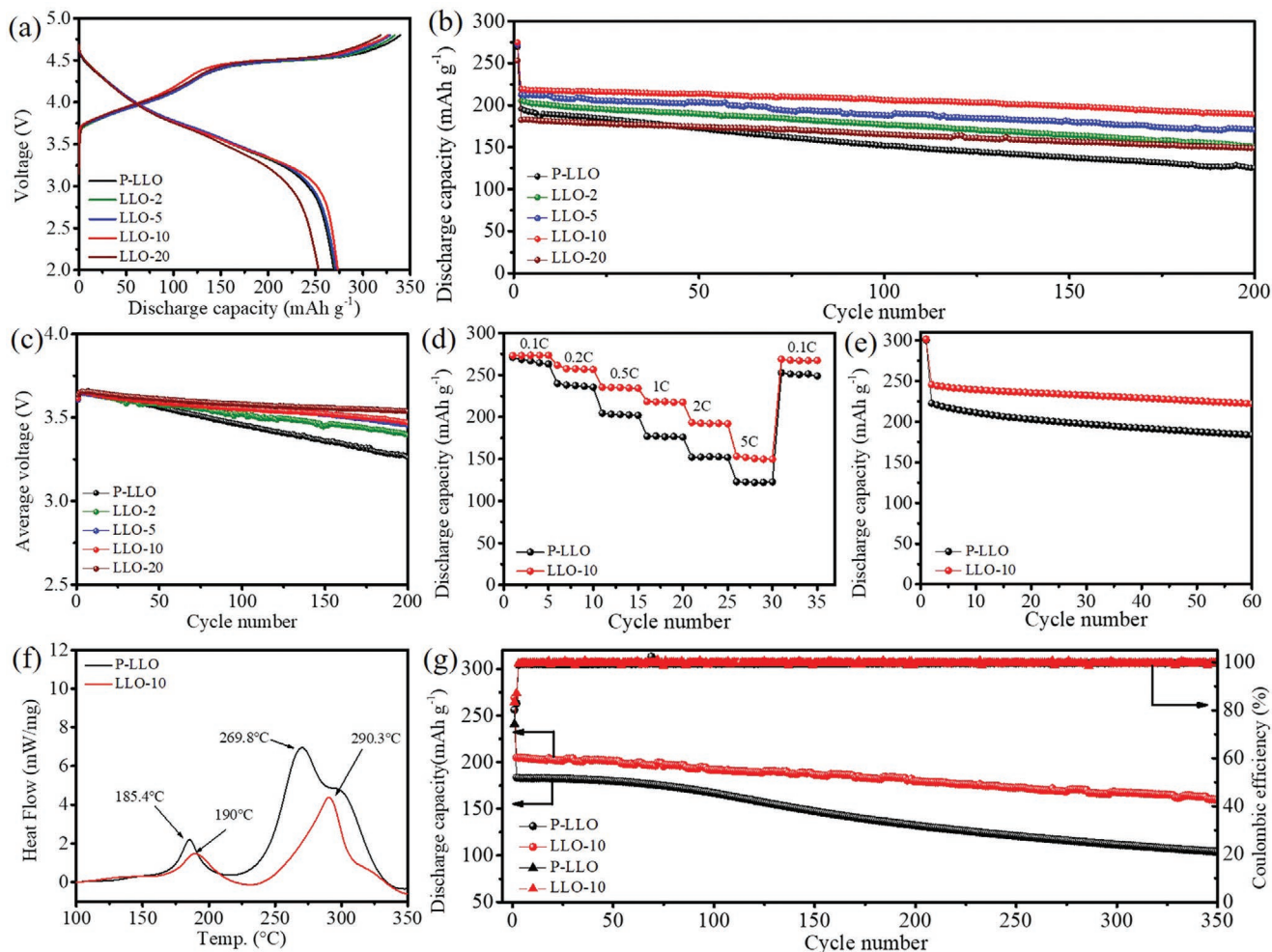


Figure 3. a) Initial charge–discharge curves of P-LLO and LLOs- n ($n = 2, 5, 10$, or 20) at 0.1 C and $25\text{ }^\circ\text{C}$. b) Long-cycle performance of the cathodes at 1 C and $25\text{ }^\circ\text{C}$. c) The plots of average discharge voltage vs. cycles. d) The rate performance and e) cycle performance of P-LLO and LLO-10 at 1 C and $55\text{ }^\circ\text{C}$. f) DSC results of P-LLO and LLO-10 after charged to 4.8 V . g) Long-cycle performance of the graphite/P-LLO and graphite/LLO-10 full cells at $25\text{ }^\circ\text{C}$.

electrochemistry, the electrochemical impedance spectroscopy (EIS) of P-LLO and LLO-10 was conducted at a charged state of 4.3 V after different cycles at frequencies ranging from 1 mHz to 100 kHz . The corresponding Nyquist plots of the electrodes are displayed in Figure S14a,b, Supporting Information. It can be seen that all the curves possess a similar feature consisting of three regions including a high-frequency semicircle, a mid-frequency semicircle and a sloping line. Basically, the intercept of EIS in the high-frequency region refers to the ohmic resistances (R_o). The semicircle in the high-frequency range is associated with the resistance (R_e) attributed to the lithium ion diffusion through the CEI film, the semicircle in the mid-frequency is attributed to the charge-transfer resistance (R_{ct}) in the electrode/electrolyte interface as well as a constant phase element, and the sloping line in the low-frequency region is associated with Warburg resistance.^[5,13,38] An equivalent circuit model was used to fit the experimental EIS results (Figure S14c, Supporting Information). Upon cycling, the mid-frequency semicircle increased significantly, indicating the decreased rate of charge transport across the CEI. Comparing the R_{ct} after 100 cycles (insets for the R_{ct} of P-LLO and LLO-10 in

Figure S14a,b, Supporting Information, respectively), although R_{ct} for LLO-10 also increases with increased cycles number, the increased value is smaller than those of P-LLO, suggesting the interface stabilization by the composite nanostructure modification. In order to exclude the influence of impedance from the anode, we also tested EIS by three-electrodes system. Although R_{ct} is reduced compared to the test by two-electrodes system (Figure S15, Supporting Information), the increase trends of R_{ct} are similar. The increase of R_{ct} has been ascribed to the formation of high-resistance products from the decomposition of electrolyte at high voltages, which is closely related to their unstable microstructure.^[5] Therefore, the suppressed impedance increase of LLO-10 during cycling demonstrates that the composite nanostructure modification could effectively restrict parasitic reactions.

The Li^+ diffusion coefficient is an important kinetic parameter for electrode materials.^[5,39–45] To gain further insight into the effect of composite nanostructure modified structure on the electrochemical performance of LLOs, galvanostatic intermittent titration technique (GITT) was applied to determine the Li^+ diffusion coefficient. The cells were galvanostatically charged

and discharged at 20 mA g⁻¹ between 2.0 and 4.8 V at 25 °C. The high overpotential is related to the kinetic-controlled steps and concentration-induced polarization during the Li⁺ extraction/insertion reaction. LLOs show a very different behavior from conventional cathode materials such as LiCoO₂.^[46,47] The larger overpotential observed in the second charge plateau (voltage >4.4 V) implies that the Li⁺ extraction reaction from Li₂MnO₃ crystal domain is kinetically limited, in agreement with our previous conclusion (Figure S16a, Supporting Information).^[48] Noticeably, the polarization of cathode can be alleviated by the modified composite nanostructure (Figure S16b, Supporting Information), indicating that the LiTaO₃ layer and spinel interlayer structure enhanced the kinetic process of the Li⁺ diffusion capability of LLO, which is in good agreement with the calculated result in Figure 1. On the basis of GITT results, the Li⁺ diffusion coefficient of Li_{1.13}Mn_{0.517}Ni_{0.256}Co_{0.097}O₂ can be calculated by the Fick's second law using Equation (1):

$$D_{\text{Li}^+} = \frac{4}{\pi} \left(\frac{m_B V_M}{M_B S} \right)^2 \left(\frac{\Delta E_S}{\Delta E_T} \right)^2 \left(\tau = \frac{L^2}{D_{\text{Li}^+}} \right) \quad (1)$$

where m_B and M_B are the molecular weight and mass of the cathode material, respectively, V_M is the molar volume of Li_{1.13}Mn_{0.517}Ni_{0.256}Co_{0.097}O₂, which is 19.84 cm³ mol⁻¹ as derived from the crystallographic data, S is the active surface area of the electrode, which is 7.62 m² g⁻¹ for P-LLO and 4.53 m² g⁻¹ for LLO-10, and L is the thickness of the electrode. Figure S16c,d, Supporting Information show variation in the Li⁺ diffusion coefficient (D_{Li^+}) as a function of OCV in the first cycle. It can be seen that all samples show similar trends of D_{Li^+} . Specifically, P-LLO shows D_{Li^+} values to be $\approx 1.0 \times 10^{-14}$ cm² s⁻¹ when OCV

is <4 V, which then decreases when OCV is >4.5 V due to the plateau charging process. The extremely small D_{Li^+} values in the plateau region indicate that the electrochemical reactions are severely sluggish, probably attributed to the high kinetic barriers associated with the Li⁺ extraction, oxygen oxidation, and structural rearrangement.^[41] In contrast, D_{Li^+} of LLO-10 is higher than that of P-LLO, indicating that the LiTaO₃ layer and spinel interlayer structure promote the electrochemical kinetics. Similarly, the D_{Li^+} of LLO-10 is higher than that of P-LLO in the second cycle, further indicating the enhancement of electrochemical kinetics by composite nanostructure modification (Figure S16e,f, Supporting Information). In addition, according to the Randle–Sevcik equation, the D_{Li^+} values of P-LLO and LLO-10 were measured by CV at different scan rates (Figure S17 and Table S2, Supporting Information), which is in good agreement with the results obtained by GITT.

To understand the mechanism of the improved interfacial stability by ALD coating, the structure of LLO-10 were compared with that of P-LLO after 200 cycles using a series of characterizations. As seen from the SEM image in Figure 4a, P-LLO particles underwent severe crackings owing to the surfacial and intergranular corrosion, likely by the acidic compounds such as HF derived from the decomposition of electrolyte. In contrast, LLO-10 could maintain the integrity and smoothness of the particle very well even after 200 cycles, as shown in Figure 4b and Figure S18, Supporting Information. It indicates that the LiTaO₃ layer and spinel interlayer structure can effectively protect the cathode against surface corrosion and cracking. The crystalline structures of P-LLO and LLO-10 after 200 cycles were further examined by ex situ XRD, Figure 4c. It can be seen that the (006)/(102) and (018)/(110)

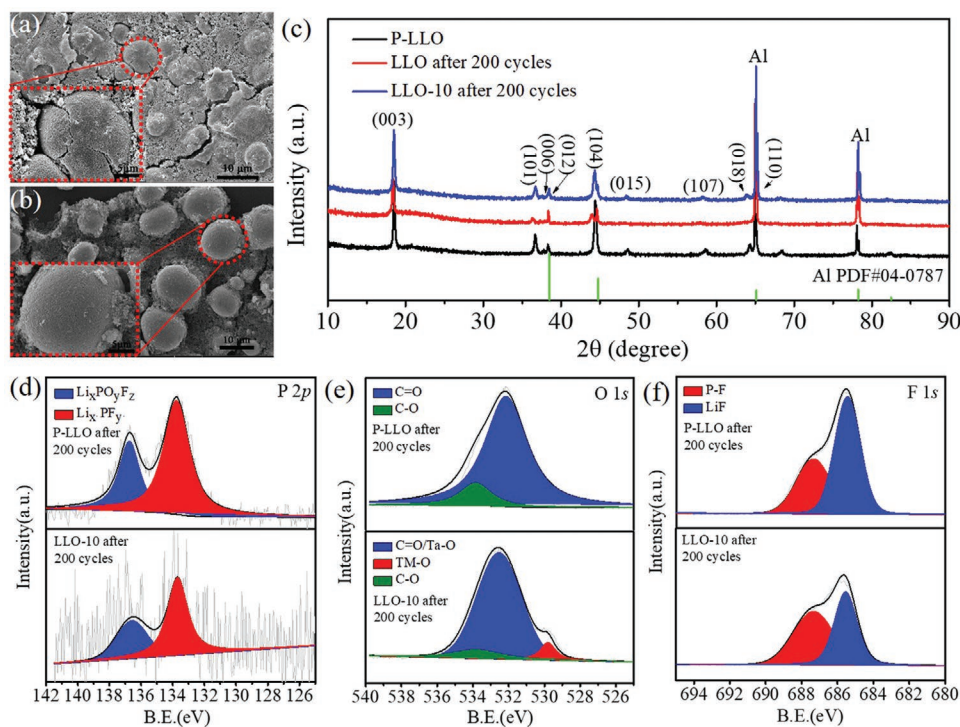


Figure 4. a,b) SEM of the P-LLO (a) and LLO-10 (b) after 200 cycles at 1 C and 25 °C. c) XRD patterns of the uncycled and cycled P-LLO and LLO-10 after 200 cycles. d–f) Comparison of the XPS spectra of P 2p (d), O 1s (e), and F 1s (f) of the P-LLO and LLO-10 after 200 cycles.

diffraction peaks of P-LLO almost disappeared after 200 cycles, suggesting the deterioration of its layered structures. However, the (006)/(102) and (018)/(110) diffraction peaks of LLO-10 still remained and kept splitting, the same as the non-cycled LLO-10. Most importantly, the downshift of (003) peak, a signal indicating the destruction of crystal structure, was considerably reduced for LLO-10 compared with P-LLO (Figure S19, Supporting Information). It is known that surface corrosion and particle cracking hinder the diffusion of Li^+ and lead to the secession of the cathode, and thus significantly reduce the rate performance and cycling stability of cathodes. Both the SEM and XRD studies indicate that the LiTaO_3 layer and spinel interlayer structure can effectively suppress the degradation of both the surface and interior structure of the cathode, and therefore the enhanced rate performance and long-cycle performance of LLO-10 were obtained.

To get a deeper insight into the effect of composite nanostructure modification on LLOs surface, the electrochemical reactions at electrode surfaces and the corresponding transformation of electrolytes should be disclosed. Toward this goal, the chemical structures of P-LLO and LLO-10 after 200 cycles were investigated by XPS (Figure 4d–f). The two typical P 2p peaks at 133.7 and 136.5 eV in Figure 4e show the existence of $\text{Li}_x\text{PO}_y\text{F}_z$ and Li_xPF_y (formed through the LiPF_6 hydrolysis) for both cathodes, respectively.^[49] However, compared with P-LLO, LLO-10 exhibits much weaker $\text{Li}_x\text{PO}_y\text{F}_z$ and Li_xPF_y peaks, indicating the deposition of the LiPF_6 electrolyte is largely suppressed by the ALD coating. The O 1s spectra of cycled P-LLO and LLO-10 are also different as seen in Figure 4e. The TM-O peak is not observed in P-LLO cathode, which means the parasitic reaction-induced passivation film is too thick to favor the XPS detection of the interior P-LLO structures. In contrast, the TM-O peaks of LLO-10 can be clearly seen, suggesting the passivation film is very thin (probably below 10 nm since the detection depth of our XPS is around 10 nm). It was previously proposed that the presence of LiF significantly increase the interfacial impedance and thus accelerates the degradation of the electrode. The F 1s spectra for of the CEI films for P-LLO and LLO-10 after 200 cycles (Figure 4f) indicate the formation of LiF as well as $\text{Li}_x\text{PO}_y\text{F}_z$, which is likely associated with the decomposition of LiPF_6 to form HF. However, it can be clearly seen that the LiF fraction of LLO-10 is significantly lower than that of P-LLO after 200 cycles, suggesting the LiTaO_3 layer and spinel interlayer structure can restrict the accessibility of HF to the cathode surface. It clearly shows that the ALD induced composite nanostructure modification as Li^+ conductive layers can improve the interfacial electrochemical stability from the decomposition parasitic reactions of electrolytes.

To summary, we have employed the industrial applicable atomic layer deposition (ALD) to fabricate composite nanostructures comprising of a Li^+ conductive LiTaO_3 layer and a spinel interlayer structure to modify the grain surface of a Li-rich layered oxide (LLO, $\text{Li}_{1.13}\text{Mn}_{0.517}\text{Ni}_{0.256}\text{Co}_{0.097}\text{O}_2$) agglomerated sphere cathode for enhanced electrochemical performance. A series of structure investigations including the advanced atomic-resolution HAADF-STEM illustrate that the formation of the ultrathin spinel interlayer structure (≈ 1 nm) grown along the [120] direction of the LLO and the well-defined, ultrathin (≈ 3 nm), and ultra-uniform Li^+ conductive LiTaO_3

layer, while XPS confirms the chemical component of LiTaO_3 for the coating layer and the valences of associated elements. The electrochemical performances of the as-prepared cathodes are found to be dependent on the ALD cycle numbers, and an optimal cathode after 10 ALD cycles can provide a very small voltage decay rate of 0.9 mV per cycle, a reversible capacity of 272.8 mAh g^{-1} at 0.1 C, a capacity retention of 85% after 200 cycles at 1 C, and a promising thermal stability. EIS, GITT and XPS were used to monitor the structure of representative materials at different electrochemical stages, which demonstrate the surface composite nanostructure can improve the electrochemical kinetics and structural/interfacial stability of the pristine LLO, and thus significantly improve the cycle stability, rate performance, thermal stability, and voltage maintenance of the cathode. This delicate and high-throughput surface strategy based on crystal domain design is anticipated to be useful for the fabrication of homogeneous, stable, and ion conductive interfaces for practical cathode materials.

Experimental Section

Synthesis of $\text{Li}_{1.13}\text{Mn}_{0.517}\text{Ni}_{0.256}\text{Co}_{0.097}\text{O}_2$: The pristine LLO of $\text{Li}_{1.13}\text{Mn}_{0.517}\text{Ni}_{0.256}\text{Co}_{0.097}\text{O}_2$ was synthesized by a co-precipitation method. First, an aqueous solution of $\text{MnSO}_4 \cdot 4\text{H}_2\text{O}$, $\text{NiSO}_4 \cdot 6\text{H}_2\text{O}$, and $\text{CoSO}_4 \cdot 7\text{H}_2\text{O}$ with a molar ratio of 0.594:0.294:0.112 and a total SO_4^{2-} concentration of 2.0 mol L^{-1} was added into a tank reactor (CSTR, 2 L in volume) under stirring. A 2.0 mol L^{-1} solution of stoichiometric Na_2CO_3 and a certain amount of 0.2 mol L^{-1} NH_4OH solution was added into the reactor at the same time. The co-precipitation temperature was maintained to be 55 °C, and the pH value was kept to be 7.8 by NH_4OH . A co-precipitated $\text{Mn}_{0.594}\text{Ni}_{0.294}\text{Co}_{0.112}\text{CO}_3$ was thus obtained, which was then washed with distilled water for several times and dried in vacuum at 80 °C for 24 h. The $\text{Mn}_{0.594}\text{Ni}_{0.294}\text{Co}_{0.112}\text{CO}_3$ precursor was grinded with Li_2CO_3 (3% Li in excess), and the mixture was pre-heated at 500 °C for 5 h and then calcined at 900 °C for 12 h in air. After cooling, the pristine $\text{Li}_{1.13}\text{Mn}_{0.517}\text{Ni}_{0.256}\text{Co}_{0.097}\text{O}_2$ micro-spherical sample was obtained, denoted as P-LLO.

ALD Coating of LiTaO_3 : The ALD coating of LiTaO_3 onto LLO was carried out in an ALD reactor (Savannah 100, Cambridge Nanotechnology Inc., USA) at 235 °C in N_2 atmosphere. In each cycle, Li_2O was first coated by pulsing and purging lithium tert-butoxide (LiOtBu , $(\text{CH}_3)_3\text{COLi}$) at 170 °C and H_2O at room temperature for one time, and Ta_2O_5 was then coated by pulsing and purging tantalum ethoxide ($\text{Ta}(\text{OEt})_5$, $\text{Ta}(\text{OC}_2\text{H}_5)_5$) at 170 °C and H_2O at room temperature for six times. The pulsing/purging time of LiOtBu , $\text{Ta}(\text{OEt})_5$, and H_2O was 1 s/15 s, 0.5 s/15 s, and 1 s/20 s, respectively. The thickness of LiTaO_3 layers was controlled by varying the number of ALD cycles (2, 5, 10 or 20), denoted as LLOs- n ($n = 2, 5, 10$ or 20).

Characterizations: The morphologies of the materials were investigated by SEM (Sirion 2000, FEI) in conjunction with EDS (Horiba, EX-250). XRD data were recorded between 10° and 90° using a Bruker D8 Advance X-ray Diffractometer with a $\text{Cu K}\alpha$ radiation. TEM was conducted on an aberration-corrected JEOL JEM-ARM200CF STEM equipped with a 200 keV Schottky cold field emission gun and HAADF detectors. The chemical valence states of materials were examined by XPS (Physical Electronics PHI model 5700 instrument with an Al X-ray source, 225 W, 15 mA, 15 kV).

The DFT^[50,51] calculations were conducted with the Vienna ab initio simulation package.^[52] The potentials were of the projector augmented wave type, and the exchange-correlation part of the density functional was treated within the generalized gradient approximation of Perdew–Burke–Ernzerhof.^[53] All structures were relaxed, until the self-consistent force was less than 10^{-2} eV \AA^{-1} . The cutoff energy for the plane-wave basis was 520 eV, and the k-point meshes were set as $3 \times 3 \times 3$ and

$3 \times 2 \times 2$ for the LiMn_2O_4 and Li_2MnO_3 models. The transition-state was studied by CI-NEB method. The Hubbard U value for Mn^{4+} is 5.0 eV.^[54]

Electrochemical Measurements: To prepare the cathodes, the active material (80 wt%) was mixed with acetylene black (15 wt%) and polyvinylidene fluoride (5 wt%) in *N*-methyl-2-pyrrolidone to produce a slurry, which was then pasted on an Al foil and dried in a vacuum oven at 80 °C overnight. The Li foil, Celgard-2400 film and 1 M LiPF_6 solution in ethylene carbonate/dimethyl carbonate (1:1 by volume) were used as the anode, separator and electrolyte, respectively. The mass loading of the active material was around 2.2 mg cm^{-2} . In the full-cell configuration, the anode electrodes were consisted of 70 wt% Graphite, 20 wt% Super P, and 10 wt% aqueous binder (CMC). Type-2032 coin cells were assembled in an argon-filled glovebox with the concentrations of H_2O and O_2 below 0.01 ppm. Charge–discharge cycling of half cells was performed at 25 °C on a LAND CT2001C (Wuhan, China) testing systems between 2.0 and 4.6 V. At first, the graphite electrode was operated inside a half cell for one cycle at 20 mA g^{-1} (0.01–3 V), with a lithium foil as the counter electrode to complete the pre-lithiation process. Then, the electrochemical evaluation was performed in a full cell with the pre-lithiation graphite as the anode electrode and P-LLO, LLO-10 as working electrodes. The full cells (1.1 ± 0.2 N/P capacity ratio) were tested between 2.0 and 4.55 V. GITT was measured on a Solartron Analytical instrument. EIS was recorded using an electrochemical workstation (CHI 660 E, Shanghai, China) at frequencies ranging from 10^{-2} to 10^5 Hz below 5 mV.

Supporting Information

Supporting Information is available from the Wiley Online Library or from the author.

Acknowledgements

E.W., Y.Z., and D.X. contributed equally to this work. This work was financially supported by the Beijing Natural Science Foundation (JQ19003), National Natural Science Foundation of China (Grants 51622202, U1507107, 21603009, and 21875007), the (National Basic Research Program of China (973 Program)) National Key R&D Program of China (Grant No. 2018YFB0104302), Project of Youth Talent Plan of Beijing Municipal Education Commission (CIT&TCD201804013) and Beijing Natural Science Foundation (KZ201910005002 and L182009).

Conflict of Interest

The authors declare no conflict of interest.

Keywords

composite nanostructure, grain surface, Li-rich layered oxides, LiTaO_3 layer, lithium ion batteries, spinel interlayer structure

Received: September 16, 2019

Revised: September 30, 2020

Published online:

- [1] R.-P. Qing, J.-L. Shi, D.-D. Xiao, X.-D. Zhang, Y.-X. Yin, Y.-B. Zhai, L. Gu, Y.-G. Guo, *Adv. Energy Mater.* **2016**, *6*, 1501914.
[2] H. J. Yu, H. S. Zhou, *J. Phys. Chem. Lett.* **2013**, *4*, 1268.
[3] M. M. Thackeray, S.-H. Kang, C. S. Johnson, J. T. Vaughney, R. Benedek, S. A. Hackney, *J. Mater. Chem.* **2007**, *17*, 3112.

- [4] H. J. Yu, P. He, H. S. Zhou, *J. Mater. Chem.* **2012**, *22*, 15507.
[5] H. J. Yu, Y. R. Wang, D. Asakura, E. Hosono, H. S. Zhou, *RSC Adv.* **2012**, *2*, 8797.
[6] Y. Zhao, J. T. Liu, S. B. Wang, R. Ji, Q. B. Xia, Z. P. Ding, W. F. Wei, Y. Liu, P. Wang, D. G. Ivey, *Adv. Funct. Mater.* **2016**, *26*, 4760.
[7] H. J. Yu, Y. G. So, Y. Ren, T. H. Wu, G. C. Guo, R. J. Xiao, J. Lu, H. Li, Y. B. Yang, H. S. Zhou, R. Z. Wang, K. Amine, Y. Ikuhara, *J. Am. Chem. Soc.* **2018**, *140*, 15279.
[8] G. Sun, F.-D. Yu, L.-F. Que, L. Deng, M.-J. Wang, Y. S. Jiang, G. J. Shao, Z.-B. Wang, *Nano Energy* **2019**, *66*, 104102.
[9] J. Shim, R. Kostecki, T. Richardson, X. Song, K. A. Striebel, *J. Power Sources* **2002**, *112*, 222.
[10] L. Yang, M. Takahashi, B. F. Wang, *Electrochim. Acta* **2006**, *51*, 3228.
[11] S. M. Zhang, H. T. Gu, H. G. Pan, S. H. Yang, W. B. Du, X. Li, M. X. Gao, Y. F. Liu, M. Zhu, L. Z. Ouyang, D. C. Jian, F. Pan, *Adv. Energy Mater.* **2017**, *7*, 1601066.
[12] A. Kapylov, J. H. Song, A. Missiul, D. J. Ham, D. H. Kim, S. Moon, J. H. Park, *ChemPhysChem* **2017**, *18*, 116.
[13] M. Zubair, G. Y. Li, B. Y. Wang, L. Wang, H. J. Yu, *ACS Appl. Energy Mater.* **2019**, *2*, 503.
[14] J. L. Shi, D.-D. Xiao, M. Y. Ge, X. Q. Yu, Y. Chu, X. J. Huang, X.-D. Zhang, Y.-X. Yin, X.-Q. Yang, Y.-G. Guo, L. Gu, L.-J. Wan, *Adv. Mater.* **2018**, *30*, 1705575.
[15] S. H. Guo, H. J. Yu, P. Liu, X. Z. Liu, D. Li, M. W. Chen, M. Ishidab, H. S. Zhou, *J. Mater. Chem. A* **2014**, *2*, 4422.
[16] W. Liu, P. Oh, X. E. Liu, S. Myeong, W. Cho, J. Cho, *Adv. Energy Mater.* **2015**, *5*, 1500274.
[17] X. Zhang, H. J. Yu, *Acc. Chem. Res.* **2020**, *53*, 368.
[18] H. J. Yu, Y.-G. So, A. Kuwabara, E. Tochigi, N. Shibata, T. Kudo, H. S. Zhou, *Nano Lett.* **2016**, *16*, 2907.
[19] Y. Z. Wang, L. Wang, X. W. Guo, T. H. Wu, Y. B. Yang, B. Y. Wang, E. R. Wang, H. J. Yu, *ACS Appl. Mater. Interfaces* **2020**, *12*, 8306.
[20] L. Wang, J. L. Shi, H. Su, G. Y. Li, M. Zubair, Y. G. Guo, H. J. Yu, *Small* **2018**, *14*, 1800887.
[21] M. T. Si, D. D. Wang, R. Zhao, D. Pan, C. Zhang, C. Y. Yu, X. Lu, H. L. Zhao, Y. Bai, *Adv. Sci.* **2019**, *7*, 1902538.
[22] W. Liu, X. F. Li, D. B. Xiong, Y. C. Hao, J. W. Li, H. R. Kou, B. Yan, D. J. Li, S. G. Lu, A. Koo, K. Adair, X. L. Sun, *Nano Energy* **2018**, *44*, 111.
[23] B. Qiu, J. Wang, Y. G. Xia, Z. Wei, S. J. Han, Z. P. Liu, *ACS Appl. Mater. Interfaces* **2014**, *6*, 9185.
[24] Y. Zhao, K. Zheng, X. L. Sun, *Joule* **2018**, *2*, 2583.
[25] B. Xiao, H. S. Liu, J. Liu, Q. Sun, B. Q. Wang, K. Kaliyappan, Y. Zhao, M. N. Banis, Y. L. Liu, R. Y. Li, T.-K. Sham, G. A. Botton, M. Cai, X. L. Sun, *Adv. Mater.* **2017**, *29*, 1703764.
[26] X. F. Li, J. Liu, M. N. Banis, A. Lushington, R. Y. Li, M. Cai, X. L. Sun, *Energy Environ. Sci.* **2014**, *7*, 768.
[27] X. F. Zhang, I. Belharouak, L. Li, Y. Lei, J. W. Elam, A. Nie, X. Q. Chen, R. S. Yassar, R. L. Axelbaum, *Adv. Energy Mater.* **2013**, *3*, 1299.
[28] H. Gao, J. Y. Cai, G.-L. Xu, L. X. Li, Y. Ren, X. B. Meng, K. Amine, Z. H. Chen, *Chem. Mater.* **2019**, *31*, 2723.
[29] M. M. Thackeray, S. H. Kang, C. S. Johnson, J. T. Vaughney, S. A. Hackney, *Electrochem. Commun.* **2006**, *8*, 1531.
[30] P. Lanz, C. Villevieille, P. Novak, *Electrochim. Acta* **2014**, *130*, 206.
[31] Y. Li, Y. Bai, X. X. Bi, J. Qian, L. Ma, J. Tian, C. Wu, F. Wu, J. Lu, K. Amine, *ChemSusChem* **2016**, *9*, 728.
[32] F. P. Zhao, Y. Zhao, J. Wang, Q. Sun, K. Adair, S. M. Zhang, J. Luo, J. J. Li, W. H. Li, Y. P. Sun, X. N. Li, J. W. Liang, C. H. Wang, R. Y. Li, H. Huang, L. Zhang, S. Q. Zhao, S. G. Lu, X. L. Sun, *Energy Storage Mater.* **2020**, *33*, 139.
[33] C. H. Wang, X. Li, Y. Zhao, M. N. Banis, J. W. Liang, X. N. Li, Y. P. Sun, K. R. Adair, Q. Sun, Y. L. Liu, F. P. Zhao, S. X. Deng, X. T. Lin, R. Y. Li, Y. F. Hu, T.-K. Sham, H. Huang, L. Zhang, R. Yang, S. G. Lu, X. L. Sun, *Small Methods* **2019**, *3*, 1900261.
[34] S. X. Deng, B. Q. Wang, Y. F. Yuan, X. Li, Q. Sun, K. Doyle-Davis, M. N. Banis, J. N. Liang, Y. Zhao, J. J. Li, R. Y. Li, T.-K. Sham,

- R. Shahbazian-Yassar, H. Wang, M. Cai, J. Lu, X. L. Sun, *Nano Energy* **2019**, 65, 103988.
- [35] J. W. Qian, L. Liu, J. X. Yang, S. Y. Li, X. Wang, H. L. L. Zhuang, Y. Y. Lu, *Nat. Commun.* **2018**, 9, 4918.
- [36] F. Gitmans, Z. Sitar, P. Günter, *Vacuum* **1995**, 46, 939.
- [37] J. Liu, M. N. Banis, X. F. Li, A. Lushington, M. Cai, R. Y. Li, T.-K. Sham, X. L. Sun, *J. Phys. Chem. C* **2013**, 117, 20260.
- [38] X. Li, K. J. Zhang, D. Mitlin, Z. Z. Yang, M. S. Wang, Y. Tang, F. Jiang, Y. G. Du, J. M. Zheng, *Chem. Mater.* **2018**, 30, 2566.
- [39] W. Weppner, R. A. Huggins, *J. Electrochem. Soc.* **1977**, 124, 1569.
- [40] K. Tang, X. Q. Yu, J. P. Sun, H. Li, X. J. Huang, *Electrochim. Acta* **2011**, 56, 4869.
- [41] Z. Li, F. Du, X. F. Bie, D. Zhang, Y. M. Cai, X. R. Cui, C. Z. Wang, G. Chen, Y. J. Wei, *J. Phys. Chem. C* **2010**, 114, 22751.
- [42] D. W. Dees, S. Kawachi, D. P. Abraham, J. Prakash, *J. Power Sources* **2009**, 189, 263.
- [43] K. M. Shaju, G. V. S. Rao, B. V. R. Chowdari, *Electrochim. Acta* **2004**, 49, 1565.
- [44] K. M. Shaju, G. V. S. Rao, B. V. R. Chowdari, *J. Mater. Chem.* **2003**, 13, 106.
- [45] K. M. Shaju, G. V. S. Rao, B. V. R. Chowdari, *J. Electrochem. Soc.* **2003**, 150, A1.
- [46] J. Xie, N. Imanishi, T. Matsumura, A. Hirano, Y. Takeda, O. Yamamoto, *Solid State Ionics* **2008**, 179, 362.
- [47] H. Xia, L. Lu, G. Ceder, *J. Power Sources* **2006**, 159, 1422.
- [48] H. J. Yu, H. J. Kim, Y. R. P. He Wang, D. Asakura, Y. Nakamura, H. S. Zhou, *Phys. Chem. Chem. Phys.* **2012**, 14, 6584.
- [49] Y. M. Zhu, X. Y. Luo, H. Z. Zhi, Y. H. Liao, L. D. Xing, M. Q. Xu, X. Liu, K. Xu, W. S. Li, *J. Mater. Chem. A* **2018**, 6, 10990.
- [50] P. Hohenberg, W. Kohn, *Phys. Rev. B* **1964**, 136, B864.
- [51] W. Kohn, L. J. Sham, *Phys. Rev. A* **1965**, 140, A1133.
- [52] P. E. Blöchl, *Phys. Rev. B* **1994**, 50, 17953.
- [53] J. P. Perdew, K. Burke, M. Ernzerhof, *Phys. Rev. Lett.* **1996**, 77, 3865.
- [54] Y. Koyama, I. Tanaka, M. Nagao, R. J. Kanno, *J. Power Sources* **2009**, 189, 798.